magnetochemistry

MDPI

Article

Surface Modifications of Superparamagnetic Iron Oxide Nanoparticles with Polyvinyl Alcohol and Activated Charcoal as Methylene Blue Adsorbents

Linh Doan [1,2,3]

[1] Department of Chemical Engineering, International University—Vietnam National University, Ho Chi Minh City 70000, Vietnam; dhlinh@hcmiu.edu.vn
[2] School of Chemical and Environmental Engineering, International University—Vietnam National University, Ho Chi Minh City 70000, Vietnam
[3] Nanomaterials Engineering Research & Development (NERD) Laboratory, International University—Vietnam National University, Ho Chi Minh City 70000, Vietnam

Abstract: As novel methylene blue adsorbents, polyvinyl alcohol and activated charcoal were used to modify the surface of superparamagnetic iron oxide nanoparticles. The adsorption capacity after 69 h was 26.50 ± 0.99–40.21 ± 1.30 mg/g, depending on the temperature (333.15, 310.15, and 298.15 K) and the initial concentration of methylene blue, which was between 0.017 and 0.020 mg/mL. Based on thermodynamics parameters, the adsorption process can be considered to be spontaneous endothermic physisorption. Kinetics studies show that the pseudo-second-order model was the best-fitted model. Adsorption isotherm studies show that the best-fitted models were the Langmuir, Langmuir, and Temkin and Pyzhev isotherm models when adsorbing MB at 333.15, 310.15, and 298.15 K, respectively.

Keywords: methylene blue; isotherm; kinetics; magnetic activated carbon; nanocomposites

check for updates

Citation: Doan, L. Surface Modifications of Superparamagnetic Iron Oxide Nanoparticles with Polyvinyl Alcohol and Activated Charcoal as Methylene Blue Adsorbents. *Magnetochemistry* **2023**, *9*, 211. https://doi.org/10.3390/magnetochemistry9090211

Academic Editor: Hongtao Guan

Received: 4 August 2023
Revised: 7 September 2023
Accepted: 18 September 2023
Published: 20 September 2023

Copyright: © 2023 by the author. Licensee MDPI, Basel, Switzerland. This article is an open access article distributed under the terms and conditions of the Creative Commons Attribution (CC BY) license (https://creativecommons.org/licenses/by/4.0/).

1. Introduction

Although magnetic nanoparticles have various applications [1], water treatment is one of the most common applications [2–5]. The magnetic property makes the separation processes easier, especially in solid–liquid phases [6], leading to their application in water treatment. Hence, magnetic separation processes are receiving more attention from researchers globally. Magnetic properties can be obtained from various magnetic nanoparticles (i.e., iron oxide nanoparticles—IONPs). IONPs have different types, including magnetite, superparamagnetic iron oxide nanoparticles, and Fe_3O_4 (SPION). SPION, a hydrophobic material, can be synthesized via multiple methods, of which co-precipitation is the most rapid, with the highest yield of magnetite and a facile synthesis method due to the suppression of maghemite, despite several disadvantages such as agglomeration [1,7–9]. This might be caused by kinetic factors while crystals are growing during the nucleation and oxidation processes [1,7–9].

In water treatment, the presence of SPION can ease the separation process when removing synthetic dyes from water due to their magnetic properties [6]. While SPION nanoparticles have a large surface area, the adsorption capacity of synthetic dyes (i.e., methyl orange, Congo red, and methylene blue—MB) can be enhanced significantly when carbon-based materials are introduced (i.e., activated charcoal (AC), graphene oxide, and carbon nanotubes) due to their larger surface area, chemical structure (i.e., porosity), and superior adsorption capabilities [2,10–20]. For instance, the adsorption capacity of SPION is only 45.43 mg/g, while SPION/MWCNT, SPION@Carbon sheets, SPION/graphene oxide, and SPION/expanded graphite have adsorption capacities of 48.06, 95, 280.26, and 76.2 mg/g, respectively [21–25]. Recently, as an MB adsorbent, SPION has been

modified using PVA and graphite, yielding SPION/PVA/GR [26]. However, one of the more inexpensive carbon-based materials is activated charcoal (AC). Commercial AC, one of the most used adsorbents due to its high pore value, huge surface area, high surface reactivity, and suitable pore distribution caused by the carbonization activation processes, can be produced from multiple sources of agricultural waste [27–29]. Hence, to improve the adsorption process of MB, which is a carcinogenic and toxic synthetic textile dye associated with cancer, skin disease, and mutations, modifying SPION with activated charcoal is necessary [30–32]. Removing methylene blue from wastewater is necessary to protect the environment and human health [32].

Even though the phase separation process between solid and liquid can be easy when using magnetic activated charcoal as an MB adsorbent, to enhance the rate of degradation of the pollutants and alter the physical form of the adsorbents (i.e., to a membrane or thin film), polymers such as polyvinylpyrrolidone, polyacrylonitrile, or especially polyvinyl alcohol (PVA) can be introduced into the composite [33–38]. Polymers can also affect the adsorption capacity of SPION-based MB adsorbents. For instance, SPION/chitosan/graphene oxide and SPION/PVA/chitosan/graphene oxide can have adsorption capacities of 30.01 and 36.4 mg/g, respectively [39,40].

This present study focuses on evaluating the potential of adsorbing MB onto SPION/PVA/AC materials, which can be synthesized via simple, environmentally friendly, and inexpensive methods. Moreover, using SPION/PVA/AC, there is a potential to make a magnetic thin film composite adsorb MB. Additionally, this work chose a very low initial concentration of MB to test the possibility of removing MB from diluted MB wastewater at 298.15–333.15 K. In this study, the characterization of SPION/PVA/AC and the quantitative method for adsorption experiments were adapted without any modifications similar to previous literature [26,40]. However, the surface charge of SPION was determined using zeta potential measurements. Additionally, by adapting the same methods and calculations without any modifications, as in previous publications, the adsorption kinetics (pseudo-first and pseudo-second-order, simplified Elovich), adsorption isotherm (Langmuir, Dubinin–Raduskevich, Halsey, Tempkin and Pyzhev, and Halsey), and thermodynamic properties were evaluated [26,40].

2. Material and Methods

2.1. Materials

From Xilong Scientific Co., Ltd. (Shantou, China), activated charcoal (AC) was bought. The remaining chemicals were used without any purification after being purchased from the same batch and companies as in the previous publication [26].

2.2. Synthesis

Solution A1—SPION synthesis: The synthesis process was adapted without any modifications from the previous publication [26].

Solution A2—SPION solution: Without any modifications, the SPION solution was prepared as in the previous publication [26].

Solution B—PVA solution: Without any modifications, the PVA solution was prepared as in the previous publication [26].

Solution C—AC solution: In 250 mL of deionized water, 12 g of dried AC was mixed for 1 h using sonication.

Solution D—SPION/PVA synthesis: Without any modifications, the SPION/PVA solution was prepared as in the previous publication [26].

Solution E—SPION/PVA/AC synthesis: To synthesize SPION/PVA/AC, solution C was initially mixed with solution D for 1 h. Then, the product was dried at 80 °C for 24 h.

Solution G—Methylene blue stock solution: Without any modifications, the MB solution was prepared as in the previous publication [26].

Solution H—Methylene blue diluted solution: Without any modifications, this step was adapted from the previous literature [26].

2.3. Adsorption/Loading Experiment

The adsorption/loading experiment was adapted from previous literature [26], except the aliquot was analyzed after every 25, 48, and 69 h. The adsorption experimental data were used to determine the loading/adsorption amount at equilibrium (Q_e, mg MB (g particles)$^{-1}$), the loading/adsorption capacity (%LC), the entrapment efficiency (%EE), adsorption kinetics (pseudo-first-order linear/nonlinear, pseudo-second-order linear/nonlinear, simplified Elovich), adsorption isotherm (Langmuir, Tempkin and Pyzhev, Freundlich, Halsey, and Dubinin–Raduskevich), and thermodynamics properties using equations published in the previous literature [26,40,41].

3. Results and Discussion

3.1. Characterization of Adsorbent

Adapting from previous publications, after synthesizing SPION/PVA/AC, the FE-SEM, FTIR, XRD, BET, BJH, and VSM were used to characterize the adsorbents [26,40]. Additionally, the zeta potential can determine the type of surface charge of SPION.

3.1.1. FE-SEM

As shown in Figure 1a, adapting from previous publications [26,40], the morphology of IONPs (iron oxide nanoparticles) was evaluated. The IONPs seem to be aggregated, which is similar to previous publications [1,26,40].

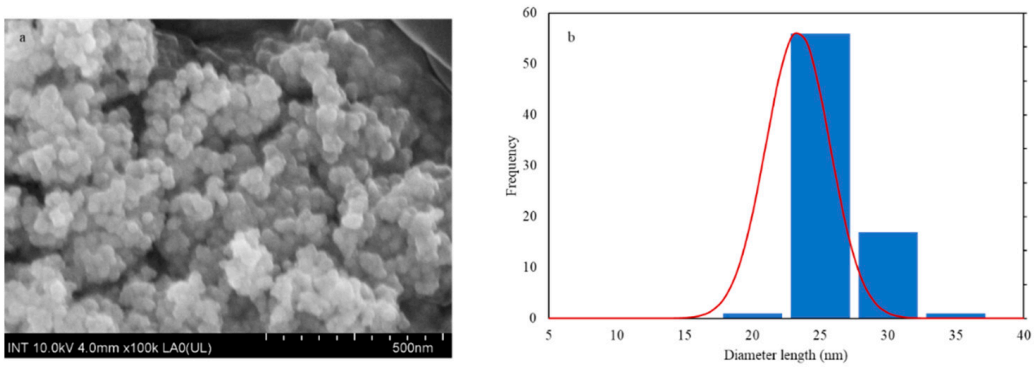

Figure 1. (**a**) FE-SEM image of IONPs. (**b**) the normal size distribution of IONPs.

Using ImageJ software v.1.53t, as shown in Figure 1b, IONPs have the mean particle size of 23.3 ± 2.4 nm. The average IONPs size matched the results of previous publications [1,26].

As shown in Figure 2a, using FE-SEM, the adsorbents, which are IONPs/PVA/AC (3:4:12 $w/w/w$), were characterized.

As shown in Figure 2a, while IONPs seem to be invisible, at the 5 µm scale, AC was clearly visible. However, as the magnification increased, in Figure 2b,c, the IONPs, which are on the surface of AC, were clearly visible. With some findings, in the area that was heavily concentrated with IONPs at 500 nm, as shown in Figure 2c, the IONPs were aggregated. This phenomenon can be explained by PVA coating the outer surface of IONPs, as demonstrated in Figure 2d. However, the aggregation can also be caused by the infamous disadvantage of the synthesis method (co-precipitation). Hence, XRD and FTIR were used to confirm Figure 2d.

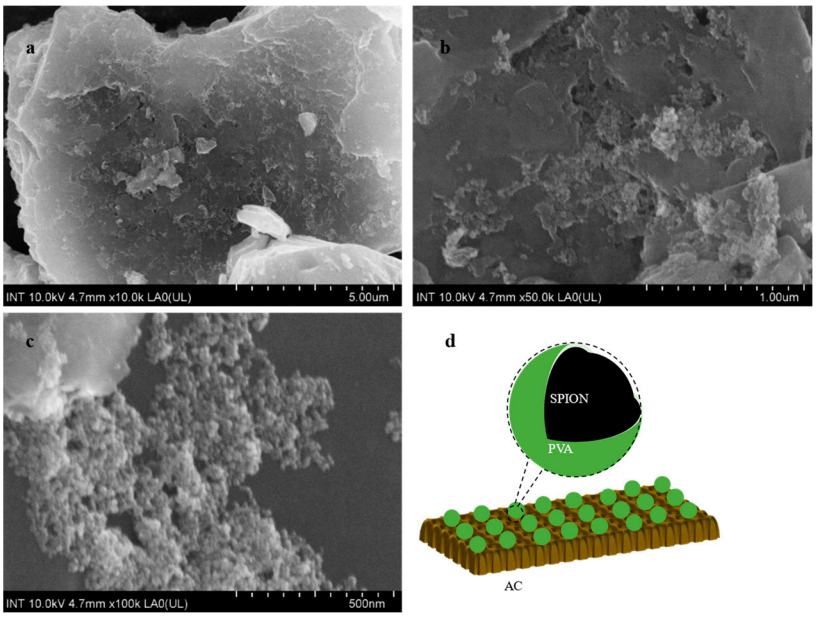

Figure 2. FE-SEM images of IONPs/PVA/AC 3:4:12 at (**a**) 5 µm, (**b**) 1 µm, (**c**) 500 nm, (**d**) the proposed structure of the adsorbents.

3.1.2. XRD Analysis

To confirm whether IONPs were SPION, XRD analysis was performed [26]. As shown in Figure 3a, the peaks at 2θ positions of 18.28°, 30.17°, 35.51°, 43.17°, 53.65°, 57.16°, and 62.75° confirm that IONPs are magnetite—SPION [42]. Moreover, the *hkl* indices that correspond to these 2θ positions are (220), (311), (400), (422), (511), and (440), which is similar to the literature [43–45].

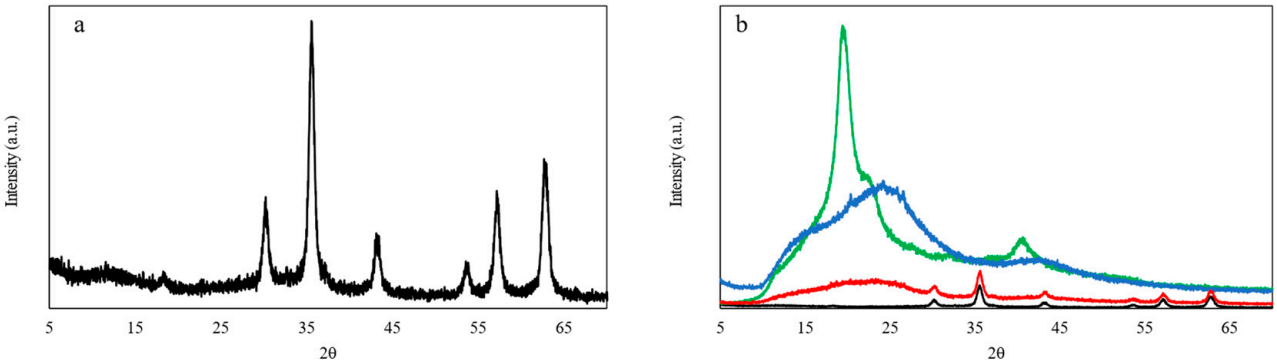

Figure 3. X-ray diffractogram of (**a**) SPION, (**b**) overlay diffractograms of SPION (black), PVA (green), AC (blue), and SPION/PVA/AC (red).

Based on Figure 3a, using the Scherrer equation at a reflective peak 2θ of 35.51° [46], the shape factor of 0.89, and the SPION size were determined to be 23.2 nm. This result corresponds to the FE-SEM analysis. As shown in Figure 3b, the peaks of SPION/PVA/AC have all the characteristic 2θ positions of SPION combining with the high-intensity peaks of AC and PVA, which indicated that SPION/PVA/AC was successfully constructed similar to Figure 2d.

3.1.3. FTIR

To determine types of bonds exists in the adsorbent, FTIR was used. The FTIR spectra were analyzed using the same instrument as the previous publication [26,40]. As seen in Figure 4, IONP were confirmed to be SPIONs due to the distinctive peaks at 584 and 446 cm^{-1} [26,40,47]. Additionally, as shown in Figure 4a, the wavelengths of 3419 and 1627 cm^{-1} also appear. These peaks were similar to previous publications [1,26,40,48–50].

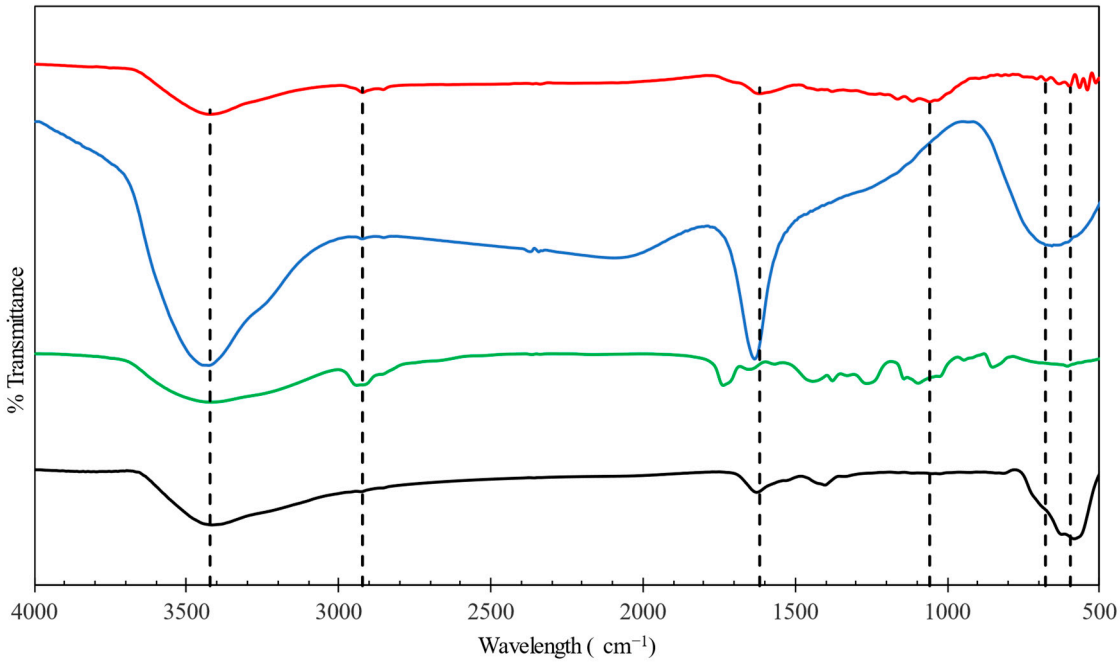

(**a**)

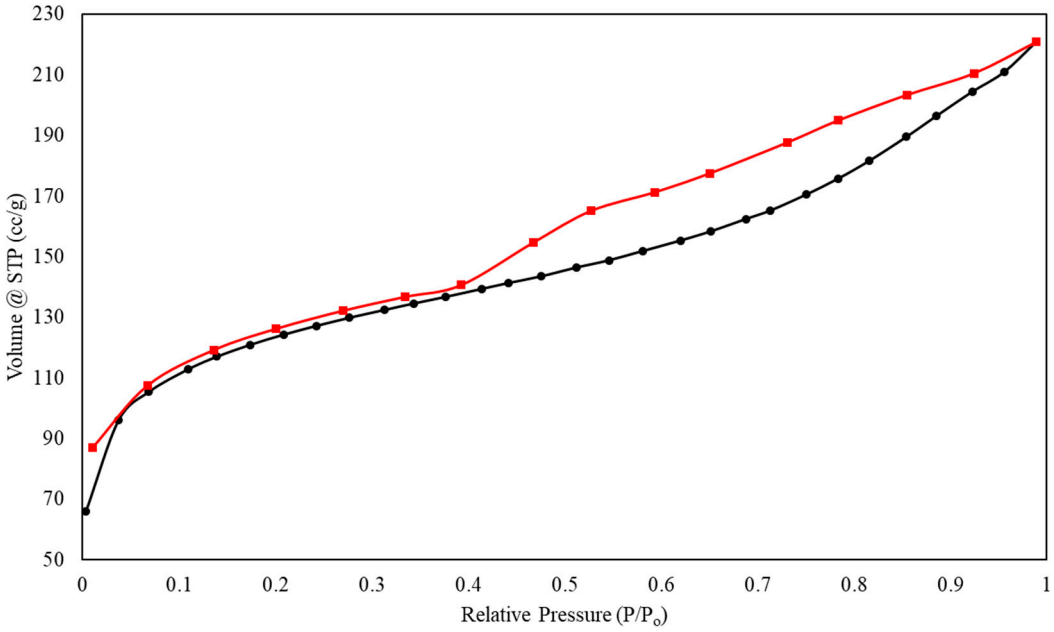

(**b**)

Figure 4. *Cont.*

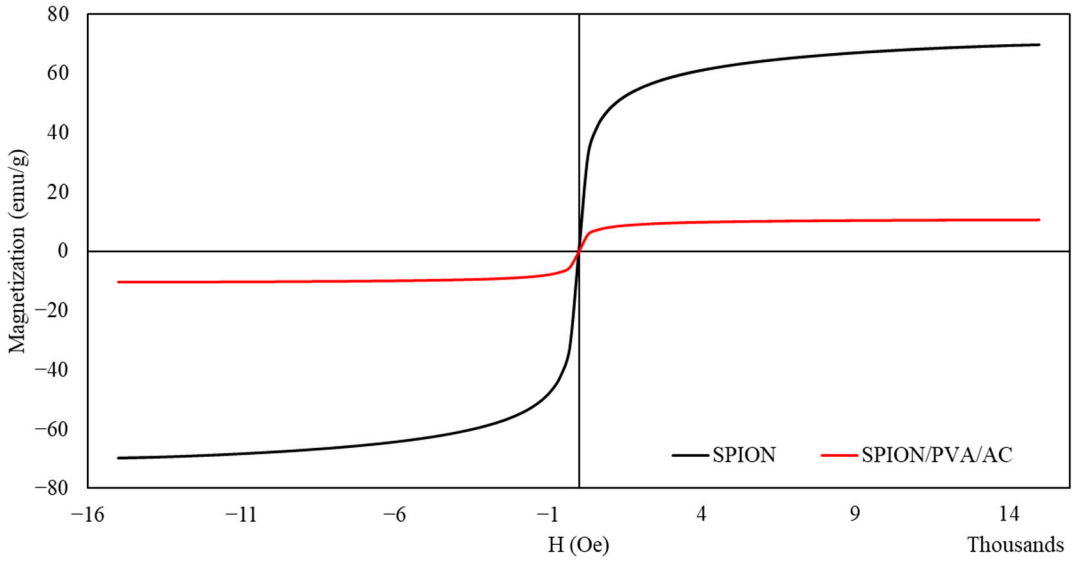

(**c**)

Figure 4. (**a**) FTIR spectra of SPION (black), PVA (green), AC (blue), and SPION/PVA/AC (red). (**b**) The BET result of relative pressure over volume of SPION/PVA/AC. (**c**) VSM result of SPION (black) and SPION/PVA/AC (red).

Additionally, as shown in Figures 3 and 4a, combining with the synthesis method similar to the literature, the IONPs that were used in this research can be considered as SPION [51–54]. As shown in Figure 4a, the PVA has peaks at 851, 1097, 1378, 1443, 1653, 1737, 2941, and 3418 cm^{-1}, which correspond to the C-C stretching vibration, C=O stretching, C-H dormation vibration, CH_2 bending, C=O carbonyl stretch, C=O stretching vibrational band, CH_2 asymmetric stretching vibration, and O-H stretching vibration, respectively [26,55–58]. As shown in Figure 4a, the AC has peaks at 1634, and 3427 cm^{-1}, which correspond to the C=O stretching vibration and the O-H stretching vibration [59]. In Figure 4a, SPION/PVA/AC has peaks at 3421, 2921, 1617, 1058, 677, 598, and 442 cm^{-1}. These peaks were similar to the peaks of SPION, PVA, and AC. Hence, Figure 2d can be considered to be the morphology of SPION/PVA/AC.

3.1.4. Zeta Potential

To evaluate one of the nanoparticles' physical properties, the zeta potential can be considered. By providing the electrical state of charged interfaces between dispersed particles, the electrostatic interaction can be measured using zeta potential [60]. The average zeta potential of SPION was 18.67 ± 6.16 mV at pH = 4–5, which was similar to other publications [61–66], and the nanoparticles were not stable in the colloid suspension [67]. However, the relationship between the zeta potential and the colloidal stability of nanoparticles in dispersion is conflicting in the literature [60]. However, based on the zeta potential reported above, the net charge of SPION nanoparticles was positive.

3.1.5. BJH Analysis

The adsorption–desorption isotherm in Figure 4b shows that starting at 0.1 p/p_o, the volume of the adsorbate uptake increases to a higher p/p_o.

From Figure 4b, a type IV isotherm can be seen. This can be interpreted that the adsorbent has a small amount of micropores (with a size between 2 and 50 nm) in its mesoporous structure [68,69]. Additionally, the hysteresis loop can be considered H3 type, indicating that the adsorbents have a wide pore size distribution [41]. As shown in Table 1, the SPION/PVA/AC's average pore diameter was shown.

Table 1. BJH and BET analyses of the SPION/PVA/AC samples.

	Adsorption
Surface area (m^2/g)	751
Pore diameter (Amstrong)	10
Pore volume (cm^3/g)	0.38

In addition to determining the surface area of 751 m^2/g, Table 1 also determines the total pore volume of the adsorbent to be 0.38 cm^3/g and the average pore diameter of the SPION/PVA/AC to be 10 Å.

3.1.6. VSM Analysis

As shown in Figure 4c, consistent with the literature, the saturation magnetization (M_s) was found to be 69.7 emu/g. This value was similar to the literature, indicating that IONPs have superparamagnetic properties [26,51,70–74].

Based on the shape of the hysteresis loop in Figure 4c, the SPION/PVA/AC can be concluded to have superparamagnetic properties as well, even though the magnetization magnitude decreases significantly compared to bare SPION from 69.7 to 10.5 emu/g. This phenomenon can be explained similar to the FE-SEM results for PVA-coated SPION [75]. From the FE-SEM, FTIR, and VSM analyses, as shown in Figure 2d, the structure of the adsorbent was proposed.

3.2. Loading Capacity of SPION/PVA/AC and Modelling

Using the same settings and instruments of UV-Vis spectrometry as in the literature, the MB concentration was quantified [26,40]. As shown in Table 2, the measured MB concentration, Q_t, %LC, and %EE of the adsorption process at 273.15, 303.15, and 333.15 K can be calculated.

Table 2. The Q_t, %LC, and %EE after 24 h of adsorption.

Initial MB Concentration (mg/mL)	**Q_t (mg/g)**	**%LC (%)**	**%EE (%)**
	333.15 K		
0.017	30.31 ± 2.51	3.03 ± 0.25	87.69 ± 4.56
0.018	29.16 ± 1.27	2.92 ± 0.13	85.39 ± 1.11
0.019	33.13 ± 2.22	3.31 ± 0.22	92.09 ± 1.42
0.020	37.48 ± 3.45	3.75 ± 0.35	94.35 ± 1.72
	310.15 K		
0.017	27.91 ± 0.41	2.79 ± 0.04	79.97 ± 2.11
0.018	28.33 ± 1.66	2.83 ± 0.17	78.95 ± 2.97
0.019	31.31 ± 1.60	3.13 ± 0.16	74.04 ± 7.38
0.020	35.04 ± 0.77	3.50 ± 0.08	81.57 ± 1.84
	298.15 K		
0.017	18.64 ± 0.79	1.86 ± 0.08	55.21 ± 2.52
0.018	21.85 ± 1.20	2.18 ± 0.12	57.91 ± 2.50
0.019	25.31 ± 0.97	2.53 ± 0.10	57.22 ± 1.78
0.020	21.75 ± 1.03	2.17 ± 0.10	56.53 ± 0.93

From Table 2, comparing to Table 1, SPION/PVA/AC has an adsorption capacity 3% higher than SPION/PVA/CS/GO [40] and SPION/CS/GO [39]. However, SPION/PVA/AC has slightly lower adsorption capacities than SPION (17.5%) [21], SPION/MWCNT (22%) [22], and SPION@Graphene (17.2%) [76]. Despite these small changes in adsorption capacity, SPION/PVA/AC consists of cheaper materials compared to SPION/CS/GO, SPION/MWCNT, and SPION@Graphene. Hence, the benefits of low cost can outweigh the slight decreases in the adsorption capacities. When compared to SPION, despite its more expensive and smaller adsorption capacities, SPION/PVA/AC consists of PVA, which can further modify the physical form of the adsorbents (i.e., thin film). Additionally, after 24 h, at 333.15 K, in four different concentrations, at least 85% methylene blue was adsorbed, while only 55% methylene blue was adsorbed at 298.15 K. This shows that as the temperature increases, the loading amount, loading capacity, and entrapment efficiency increase significantly after 24 h. Hence, temperature has significant effects on adsorption capacity.

Due to the effect of temperature, the thermodynamic parameters were calculated and are given in Table 3.

Table 3. Thermodynamic parameters after 69 h adsorption.

Temperature (K)	ΔG (J/mol)	ΔH (J/mol)	ΔS (J/mol K)
298.15	−666.14	7.11	2.26
310.15	−693.237		
333.15	−745.173		

As shown in Table 3, a feasible and spontaneous adsorption process can be interpreted by $\Delta G < 0$ [77–81]. To further interpret the ΔG value, as the temperature increases, ΔG becomes more negative. This indicates that physical forces are the main factor in the adsorption process, and adsorption is more favorable at higher temperatures [77,82]. In addition, the value of ΔS, which is greater than zero, indicates that during the adsorption process, the surface randomness increases and the MB and SPION/PVA/AC internal structures change [77–81]. Additionally, $\Delta H > 0$ indicates that the adsorption process was endothermic, there was an occurrence of monolayer adsorption, and weak chemical forces between the adsorbents and MB exist [77–81]. The endothermic adsorption process means that the adsorption degree increases as the temperature increases [80]. The endothermic adsorption can be explained by the interaction between pre-adsorbed water and SPION/PVA/AC, which is stronger than the interaction between MB and SPION/PVA/AC [83]. Hence, MB molecules have to compete for the active sites of SPION/PVA/AC against water molecules, resulting in the simultaneous adsorption–desorption of MB and water, yielding $\Delta H > 0$ [84,85]. The adsorption process can be considered to be physisorption if the $\Delta H > 40$ kJ/mol [77,80]. As shown in Table 3, as the indicator, the $\Delta H < 20$ kJ/mol shows that Van der Waals forces dominate the physisorption interaction [86]. Additionally, this value also indicates that the electrostatic interactions and forces of attraction were weak and the bonding between MB and the adsorbents was loose [87–89]. After determining the relationship between temperature and adsorption capacities, the relationship between time and adsorption capacities were investigated (as shown in Table 4).

As shown in Table 4, the adsorption capacity increased as the temperature increases from 298.15 to 310.15 K, indicating an endothermic process, which is in accord with $\Delta H > 0$ [77,78]. However, the adsorption capacity decreased insignificantly as the temperature reached 333.15 K. This phenomenon might be due to the decrease in adsorption forces between the active sites of SPION/PVA/AC and MB [90,91] and the increase in mobility of MB ions [92]. When increasing the initial MB concentration, the driving force of mass transfer is higher, leading to an increase in adsorption/loading capacity [93]. After 25 h, at a temperature of 333.15 K, the loading capacity did not deviate much. This phenomenon can be caused by a decreased ratio between the free methylene blue molecules and the abundant free adsorption sites available [92,94]. From Table 4, to have the highest adsorp-

tion capacities, SPION/PVA/AC must be in contact with MB solution at the concentration of 0.02 mg/mL for 69 h at 310.15 K. After adsorbing almost all the methylene blue (%EE was close to 100%), values of loading amount (Q_t) and time (t) were used to calculate the adsorption kinetics using multiple kinetics models.

Table 4. The Q_t, %LC, %EE after 69 h adsorption.

Initial MB Concentration (mg/mL)	Q_t (mg/g)	%LC (%)	%EE (%)
333.15 K			
0.017	33.99 ± 1.30	3.40 ± 0.13	98.46 ± 0.99
0.018	33.37 ± 1.13	3.34 ± 0.11	97.76 ± 1.00
0.019	35.45 ± 1.84	3.55 ± 0.18	98.63 ± 0.23
0.020	39.22 ± 4.03	3.92 ± 0.40	98.60 ± 0.72
310.15 K			
0.017	32.74 ± 0.42	3.27 ± 0.04	93.80 ± 0.96
0.018	33.33 ± 1.62	3.33 ± 0.16	92.89 ± 2.17
0.019	37.17 ± 0.52	3.72 ± 0.05	87.72 ± 5.54
0.020	40.21 ± 1.30	4.02 ± 0.13	93.57 ± 1.29
298.15 K			
0.017	26.50 ± 0.99	2.65 ± 0.10	78.50 ± 3.42
0.018	30.09 ± 1.69	3.01 ± 0.17	79.75 ± 3.41
0.019	34.72 ± 1.50	3.47 ± 0.15	78.50 ± 2.68
0.020	31.33 ± 0.97	3.13 ± 0.10	81.47 ± 1.07

As shown in Table 5 and Figure 5, at different adsorption conditions (i.e., temperature, time, and MB concentration), the pseudo-second-order and simplified Elovich kinetic model can determine the adsorption rate and the loading amount at equilibrium.

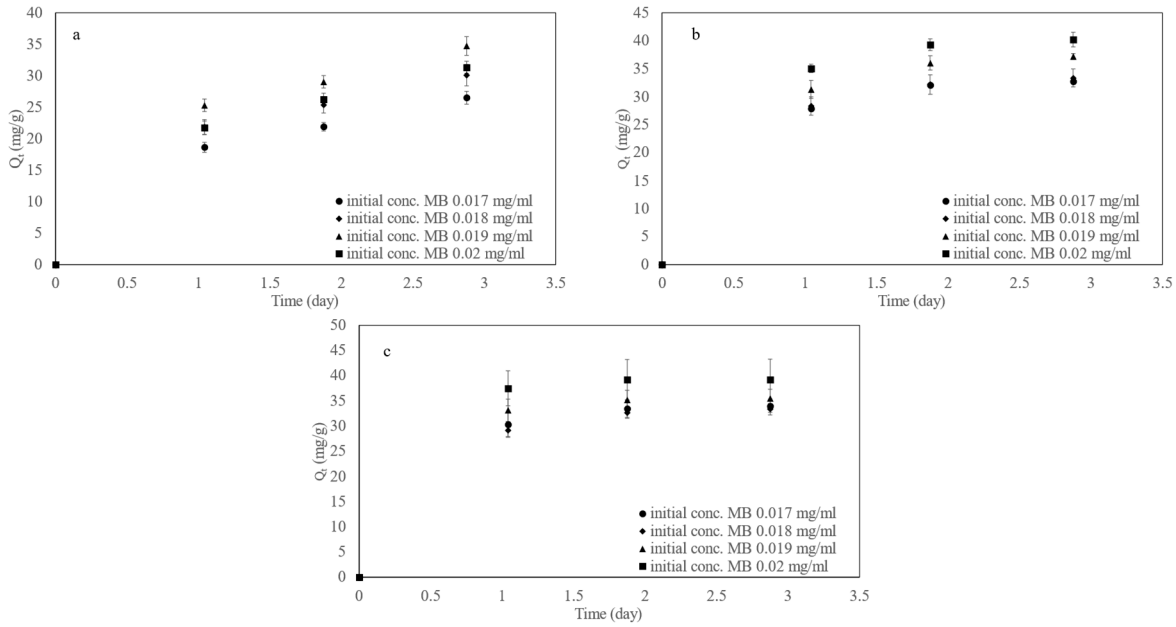

Figure 5. Adsorption capacity (mg/g) over time at (**a**) 273.15 K, (**b**) 310.15 K, (**c**) 333.15 K.

Table 5. Kinetic models after 69 h adsorption.

		Initial MB Concentration (mg/mL)			
		0.017	**0.018**	**0.019**	**0.020**
333.15 K					
Pseudo-first order	Q_e mg MB (g particles)$^{-1}$	32.61	31.99	34.61	38.65
	k_1 (g mg^{-1} min^{-1})	1.07	1.07	1.07	1.07
	χ^2	0.24	0.36	0.09	0.05
Pseudo-second order	Q_e mg MB (g particles)$^{-1}$	36.89	37.16	37.23	40.60
	k_2 (g mg^{-1} day^{-1})	0.123	0.099	0.214	0.296
	χ^2	0.008	0.034	0.005	0.005
Simplified Elovich	α (mg/(g day))	43.56	42.57	47.00	52.83
	β (mg/g)	0.050	0.047	0.047	0.042
	R^2	0.40	0.44	0.39	0.38
310.15 K					
Pseudo-first order	Q_e mg MB (g particles)$^{-1}$	30.98	31.56	34.93	38.25
	k_1 (g mg^{-1} min^{-1})	1.07	1.07	1.07	1.07
	χ^2	0.44	0.48	0.55	0.40
Pseudo-second order	Q_e mg MB (g particles)$^{-1}$	36.91	37.75	42.12	44.39
	k_2 (g mg^{-1} day^{-1})	0.083	0.079	0.068	0.083
	χ^2	0.02	0.03	0.01	0.01
Simplified Elovich	α (mg/(g day))	41.20	41.70	46.39	51.06
	β (mg/g)	0.048	0.048	0.042	0.040
	R^2	0.45	0.45	0.46	0.43
273.15 K					
Pseudo-first order	Q_e mg MB (g particles)$^{-1}$	22.58	25.35	29.94	26.73
	k_1 (g mg^{-1} min^{-1})	1.07	1.07	1.07	1.07
	χ^2	1.39	1.53	1.51	1.73
Pseudo-second order	Q_e mg MB (g particles)$^{-1}$	33.92	36.15	42.73	40.97
	k_2 (g mg^{-1} day^{-1})	0.033	0.037	0.031	0.026
	χ^2	0.07	0.34	0.10	0.05
Simplified Elovich	α (mg/(g day))	29.64	34.13	39.33	35.09
	β (mg/g)	0.056	0.050	0.044	0.047
	R^2	0.59	0.57	0.57	0.60

As shown in Table 5, at 333.15, 310.15, and 273.15 K, out of all the mentioned kinetics models, the pseudo-second order can be considered to be the most fitted for SPION/PVA/AC due to the small χ^2 and R^2 values. The pseudo-second-order kinetic model, which is shown in Table 5, indicates that the adsorption mechanism is involved in chemisorption via electrons transferring (valence forces) between MB and the adsorbent [95–99].

As the temperature increased from 273.15 to 310.15 K, the k_2 values increased as well, indicating a faster adsorption rate at high temperatures [92]. Moreover, depending on the adsorption conditions (i.e., adsorption contact time and adsorption amount), the MB adsorption rate decreases as time increases. This phenomenon can be caused by the conversion of MB to the MB^+ cationic form [77].

After 25 h, MB had a slight shift in the UV-VIS peak wavelength when the adsorption experiments were at T = 333.15 K. However, at 298.15 K and 310.15 K, the phenomenon was not seen. The wavelength shift phenomenon can be seen and explained similarly to previous publications [26].

Comparing the obtained experimental and calculated equilibrium adsorption capacities (as shown in Tables 4 and 5), these values were much smaller compared to some literature [100–108] and much greater compared to other literature [89,93,109–112]. Similar to the previous publication, as shown in Table 6, various adsorption isotherm models, including isotherm constants, were determined [26].

Table 6. Adsorption isotherms model constants and variables.

Model	Constant	298.15 K	310.15 K	333.15 K
Langmuir	k_L (L/mg)	−0.03	3	2.58
	Q^0 (mg/g)	−243.90	42.19	24.51
	Average R_L	$1.00 \pm 3 \times 10^{-5}$	0.95 ± 0.003	0.95 ± 0.003
	R^2	0.28	0.998	0.998
Freundlich	k_F (mg/g)	2.28	4.52	4.83
	$\frac{1}{n_F}$ (mg/L)	1.17	0.18	−0.28
	R^2	0.998	0.990	0.9485
Dubinin–Radushkevich	k_{DR} (mol^2 J^2)	2	0.02	−0.09
	Q_m (mg/g)	59.18	40.19	26.70
	E (kJ mol^{-1})	250	7142.86	−5555.56
	R^2	0.9794	0.9751	0.9578
Temkin and Pyzhev	B_1	37.94	6.39	−9.47
	k_{TP} (mg/g)	−0.49	5.04	−3.96
	R^2	0.999	0.990	0.938
Halsey	n	−0.85	−5.46	3.52
	k_{Ha}	5.07	1.71×10^8	2.84×10^{-6}
	R^2	0.998	0.990	0.9485

The adsorption experimental parameters can be fitted using all the above isotherm models, based on the R^2 values, except Langmuir at 298.15 K. However, as shown in Table 6, at 310.15 and 333.15 K, the best-fitted isotherm model is Langmuir due to the highest R^2 values. Similarly, at 298.15 K, the best-fitted isotherm model is Temkin and Pyzhev due to the highest R^2 value. As shown in Table 6, at 310.15 and 333.15 K, since 0 < average R_L < 1 in the Langmuir adsorption isotherm models (as shown in Figure 6), the adsorption mechanism can be described as the attachment of MB onto the surface of SPION/PVA/AC,

which is favorable [2,22]. From the Langmuir isotherm model, the adsorbent's surface can be considered to be homogeneous, and MB was adsorbed as a monolayer [25,26].

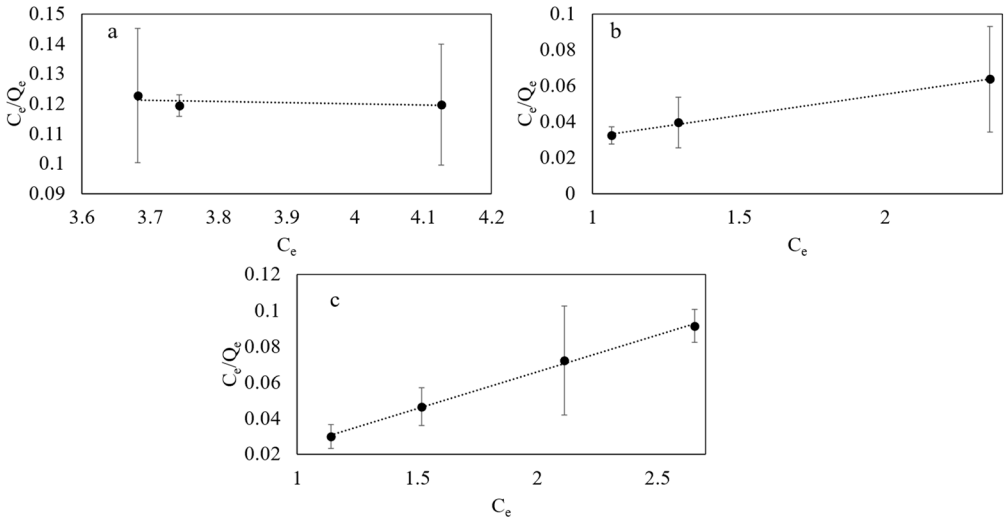

Figure 6. The Langmuir adsorption isotherm model at (**a**) 273.15 K, (**b**) 310.15 K, and (**c**) 333.15 K.

As shown in Figure 7, from the Frendlich isotherm model, at 333.15 K, the $\frac{1}{n_F}$ value indicates the non-favorable physical process [26].

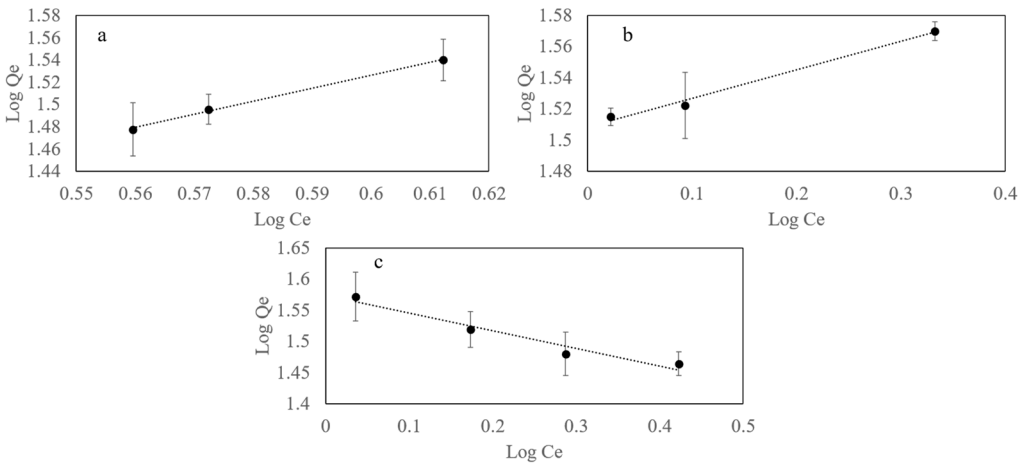

Figure 7. The Freundlich adsorption isotherm model at (**a**) 273.15 K, (**b**) 310.15 K, and (**c**) 333.15 K.

At 310.15 K, as $\frac{1}{n_F}$ is the closest to 0, the physical process was favorable. Moreover, the values of n_F, which were smaller than 1 at T = 333.15 K and 298.15 K, represent the poor adsorption characteristic, while at 310.15 K, the n_F value was greater than 1, which indicates the good adsorption characteristic [77]. Since $\frac{1}{n_F} > 1$, the adsorption process has involved cooperative adsorption [26,102,113]. Moreover, since $n_F < 1$, with surface density, the bond energies increase [26,114].

Looking at the Dubinin–Radushkevich model, as shown in Figure 8, the R^2 value was greater than 0.5, which indicates that the adsorption between SPION/PVA/AC and methylene blue occurred in relevance with this isotherm at all temperatures [115].

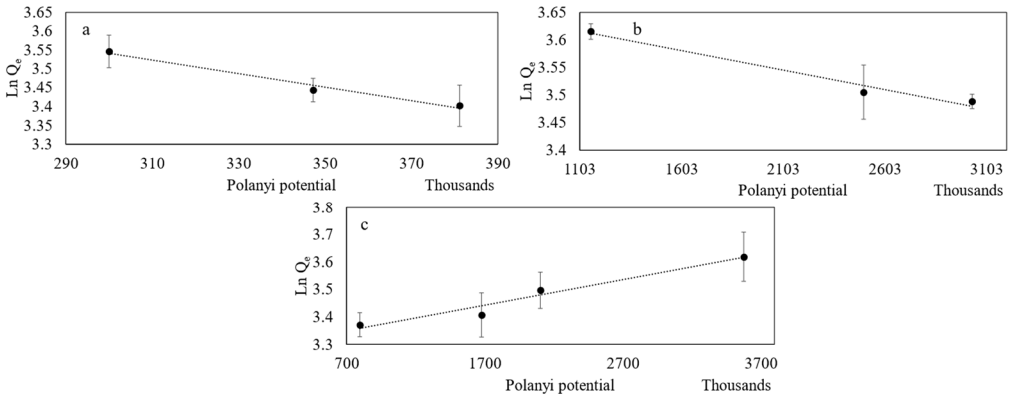

Figure 8. The Dubinin–Radushkevich adsorption isotherm model at (**a**) 273.15 K, (**b**) 310.15 K, (**c**) 333.15 K.

Since $K_{DR} < 1$, the surface heterogeneity increased due to the pore structure of SPION/PVA/AC and the interactions between SPION/PVA/AC and MB [26,116]. Because $E < 0$, the sorption process is exothermic [117]. When E is between 8 and 16 kJ/mol or $E < 8$ kJ/mol, the adsorption process that occurs can be chemical ion-exchange or physical adsorption, respectively [26,118–121]. Hence, from Figure 8, the sorption process can be considered to be physical adsorption.

On the other hand, at 298.15 K, the best-fitted adsorption isotherm model was Temkin and Pyzhev, as shown in Figure 9, with an R^2 value of 0.999.

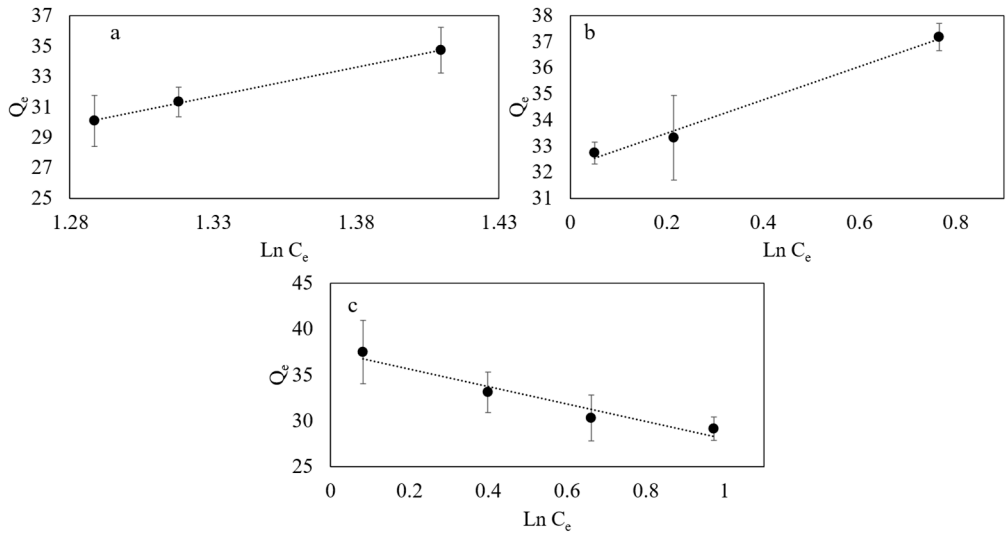

Figure 9. The Temkin and Pyzhev adsorption isotherm model at (**a**) 273.15 K, (**b**) 310.15 K, and (**c**) 333.15 K.

The Temkin and Pyzhev model shows that adsorption is characterized by a uniform distribution of binding energies, up to some maximum binding energy [122,123]

Similar to the Freundlich isotherm model, the Halsey isotherm model can examine an adsorption system that has multilayered and heterogeneous surfaces with a uniform surface heat distribution [26,124]. Hence, at 273.15 K, 310.15 K, and 333.15 K, the only model that is not the worst-fitted model is Halsey, as shown in Figure 10, and it has similar R^2 values as the Freundlich isotherm model.

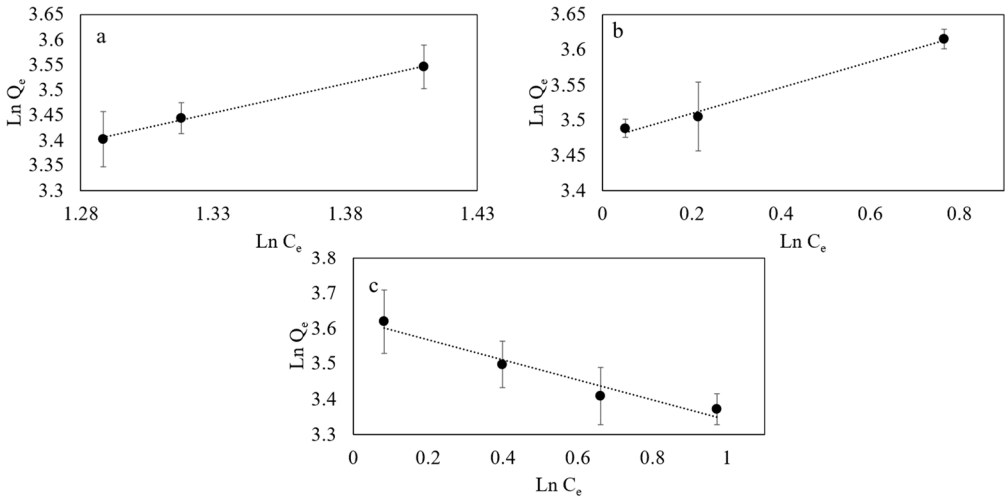

Figure 10. The Halsey adsorption isotherm model at (**a**) 273.15 K, (**b**) 310.15 K, and (**c**) 333.15 K.

As shown in Table 6, at 333.15 K, since I $\neq$ 0, the intraparticle diffusion model can be considered to be not only intraparticle diffusion but also film diffusion [26,77].

Additionally, from the data in Table 7 and Figure 11, as the k_I values decrease while temperature increases, combining with the I values, the diffusion process (intraparticle and film) happened simultaneously [125–127].

Table 7. The intraparticle diffusion model after 96 h.

Initial MB Concentration (mg/mL)	k_I	I
	298.15 K	
0.017	3.04	29.38
0.018	5.06	27.00
0.019	3.05	31.83
0.020	2.91	36.15
	310.15 K	
0.017	5.15	25.94
0.018	5.35	26.12
0.019	6.25	28.80
0.020	5.52	32.86
	333.15 K	
0.017	8.60	14.05
0.018	9.01	17.07
0.019	10.31	19.74
0.020	10.44	16.36

In addition to intraparticle diffusion, film diffusion, chemisorption, and physical adsorption, other adsorption mechanisms could include the electrostatic interaction of surface negative charge with the positively charged methylene blue, the hydrogen bonding, and the π-π* stacking with the aromatic ring of methylene blue [125–127]. Moreover, the adsorption mechanisms can be controlled by external diffusion and boundary layer diffusion [77,88,128]. Hence, the adsorption was not only controlled by the rate-control step but also by some of the kinetic models and intraparticle diffusion as well.

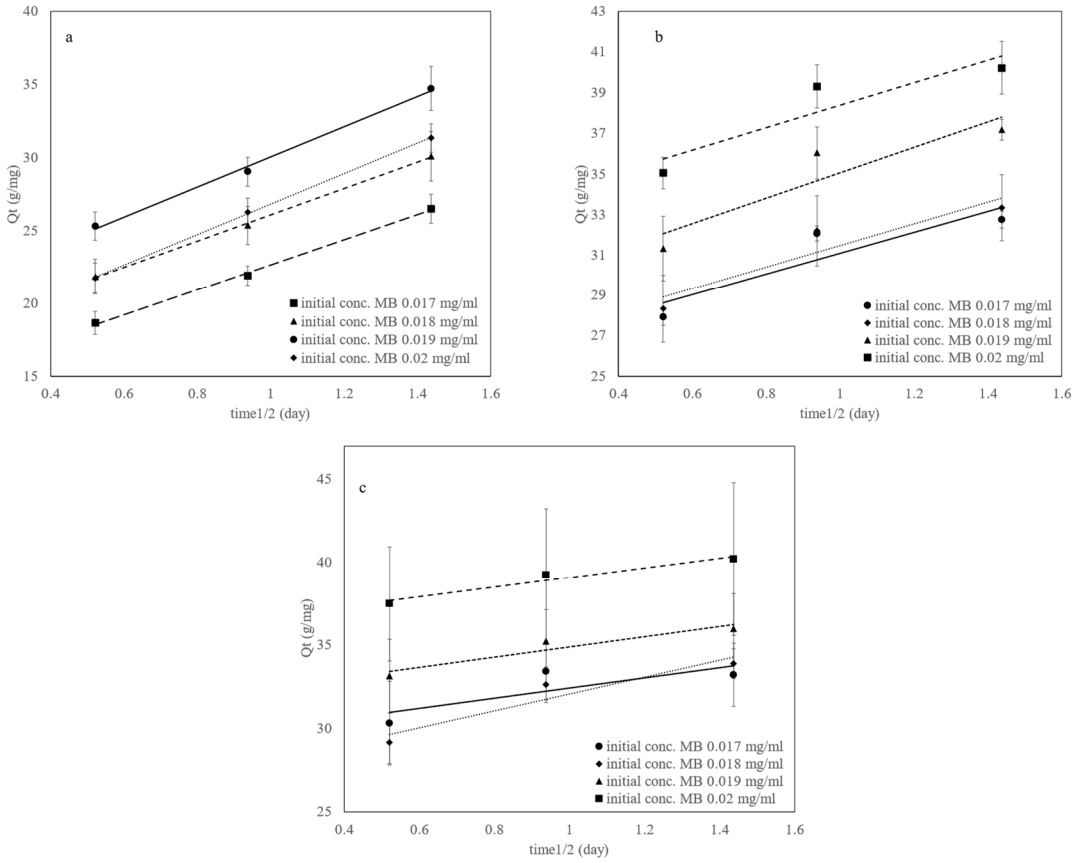

Figure 11. The intraparticle diffusion model at (**a**) 273.15 K, (**b**) 310.15 K, (**c**) 333.15 K.

4. Conclusions

Using polyvinyl alcohol and activated charcoal to modify the surface of superparamagnetic iron oxide nanoparticles, the materials can adsorb MB at 333.15, 310.15, and 298.15 K with the adsorption capacity after 69 h ranging from 26.50 ± 0.99 to 40.21 ± 1.30 depending on the temperature and the initial concentration of methylene blue, which were between 0.017 and 0.020 mg/mL. The thermodynamic parameters indicate that the adsorption was endothermic, spontaneous, and physisorption. The adsorption capacity increased as temperature increased despite the physical change of methylene blue at 333.15 K based on the shift in the UV-VIS peak wavelength. Based on the adsorption kinetics (pseudo-second order) and the intraparticle diffusion model, the adsorption mechanism can be considered chemisorption and exothermic. The Langmuir, Langmuir, and Temkin–Pyzhev isotherm models were the best-fitted models at 333.15, 310.15, and 298.15 K, respectively.

Funding: This research is funded by International University. VNU-HCM under grant number T2022-01-CEE.

Institutional Review Board Statement: Not applicable.

Informed Consent Statement: Not applicable.

Data Availability Statement: All data that support the findings of this study are included within the article.

Acknowledgments: The following undergraduate students from International University—Vietnam National University, Ho Chi Minh City, Vietnam are greatly acknowledged: Ngan T.N. Nguyen, Linh Bui, Tan Nguyen, and Tu Nguyen. The contribution of Mai V.T. Tam who affiliates to the Institute for Computational Science and Technology, Ho Chi Minh City was greatly recognized.

Conflicts of Interest: The author declare no conflict of interest.

Abbreviations

C_0	initial concentration
C_t	concentration at time t
V	reaction volume
m	mass of the nanoparticles
h_0	initial adsorption rate
Q_e	the amounts of MB (an adsorbate) adsorbed at the equilibrium
Q_t,	the amounts of MB adsorbed at time t
k_1	the pseudo-first-order rate constant
k_2	pseudo-second-order rate constant
C_e	the equilibrium aqueous-phase concentration adsorbate
Q^0	the monolayer adsorption capacity which can be understood as the theoretical adsorption capacity
K_L	the constant related to the free adsorption energy and the reciprocal of the concentration at which half saturation of the adsorbent is reached
Q_m	the quantity of adsorbate adsorbed in a single monolayer
θ	the fractional surface coverage
k_a	the respective rate constant for adsorption
k_d	the respective rate constant for desorption
$\frac{1}{n_F}$	the intensity of the adsorption
K_F	constant of the relative adsorption capacity of the adsorbent
Q_{mDR}	theoretical saturation capacity
K_{DR}	the activity coefficient related to mean free energy of adsorption
ε	the Polanyi potential
R	universal gas constant
T	temperature
K_{TP}	equilibrium binding constant
B_1	related to the heat of adsorption
K_{Ha}	the Halsey isotherm constant
k_i	intraparticle diffusion rate constant
I	constant
α	the theoretical initial adsorption rate
β	the theoretical desorption constant
ΔG	Gibbs free energy change
ΔH	standard enthalpy change
ΔS	entropy change
K_0	thermodynamic equilibrium constant in the adsorption process

References

1. Doan, L.; Lu, Y.; Karatela, M.; Phan, V.; Jeffryes, C.; Benson, T.; Wujcik, E.K. Surface Modifications of Superparamagnetic Iron Oxide Nanoparticles with Polylactic Acid-Polyethylene Glycol Diblock Copolymer and Graphene Oxide for a Protein Delivery Vehicle. *Eng. Sci.* **2019**, *7*, 10–16. [CrossRef]
2. Bayazit, Ş.S. Magnetic Multi-Wall Carbon Nanotubes for Methyl Orange Removal from Aqueous Solutions: Equilibrium, Kinetic and Thermodynamic Studies. *Sep. Sci. Technol.* **2014**, *49*, 1389–1400. [CrossRef]
3. Ge, M.; Xi, Z.; Zhu, C.; Liang, G.; Hu, G.; Jamal, L.; S. M., J.A. Preparation and Characterization of Magadiite–Magnetite Nanocomposite with Its Sorption Performance Analyses on Removal of Methylene Blue from Aqueous Solutions. *Polymers* **2019**, *11*, 607. [CrossRef]
4. Nicola, R.; Costişor, O.; Muntean, S.-G.; Nistor, M.-A.; Putz, A.-M.; Ianăşi, C.; Lazău, R.; Almásy, L.; Săcărescu, L. Mesoporous Magnetic Nanocomposites: A Promising Adsorbent for the Removal of Dyes from Aqueous Solutions. *J. Porous Mater.* **2020**, *27*, 413–428. [CrossRef]
5. Nicola, R.; Muntean, S.-G.; Nistor, M.-A.; Putz, A.-M.; Almásy, L.; Săcărescu, L. Highly Efficient and Fast Removal of Colored Pollutants from Single and Binary Systems, Using Magnetic Mesoporous Silica. *Chemosphere* **2020**, *261*, 127737. [CrossRef]
6. Altıntıg, E.; Altundag, H.; Tuzen, M.; Sarı, A. Effective Removal of Methylene Blue from Aqueous Solutions Using Magnetic Loaded Activated Carbon as Novel Adsorbent. *Chem. Eng. Res. Des.* **2017**, *122*, 151–163. [CrossRef]
7. Kim, D.K.; Zhang, Y.; Voit, W.; Rao, K.V.; Muhammed, M. Synthesis and Characterization of Surfactant-Coated Superparamagnetic Monodispersed Iron Oxide Nanoparticles. *J. Magn. Magn. Mater.* **2001**, *225*, 30–36. [CrossRef]

8. Marinin, A. Synthesis and Characterization of Superparamagnetic Iron Oxide Nanoparticles Coated with Silica. Master's Thesis, Royal Institute of Technology, Stockholm, Sweden, 2012.
9. Muthiah, M.; Park, I.-K.; Cho, C.-S. Surface Modification of Iron Oxide Nanoparticles by Biocompatible Polymers for Tissue Imaging and Targeting. *Biotechnol. Adv.* **2013**, *31*, 1224–1236. [CrossRef] [PubMed]
10. Xu, P.; Zeng, G.M.; Huang, D.L.; Feng, C.L.; Hu, S.; Zhao, M.H.; Lai, C.; Wei, Z.; Huang, C.; Xie, G.X.; et al. Use of Iron Oxide Nanomaterials in Wastewater Treatment: A Review. *Sci. Total Environ.* **2012**, *424*, 1–10. [CrossRef]
11. Duan, J.; Liu, R.; Chen, T.; Zhang, B.; Liu, J. Halloysite Nanotube-Fe_3O_4 Composite for Removal of Methyl Violet from Aqueous Solutions. *Desalination* **2012**, *293*, 46–52. [CrossRef]
12. Zhu, H.-Y.; Fu, Y.-Q.; Jiang, R.; Jiang, J.-H.; Xiao, L.; Zeng, G.-M.; Zhao, S.-L.; Wang, Y. Adsorption Removal of Congo Red onto Magnetic Cellulose/Fe_3O_4/Activated Carbon Composite: Equilibrium, Kinetic and Thermodynamic Studies. *Chem. Eng. J.* **2011**, *173*, 494–502. [CrossRef]
13. Yang, N.; Zhu, S.; Zhang, D.; Xu, S. Synthesis and Properties of Magnetic Fe_3O_4-Activated Carbon Nanocomposite Particles for Dye Removal. *Mater. Lett.* **2008**, *62*, 645–647. [CrossRef]
14. Wang, J.; Tang, B.; Tsuzuki, T.; Liu, Q.; Hou, X.; Sun, L. Synthesis, Characterization and Adsorption Properties of Superparamagnetic Polystyrene/Fe_3O_4/Graphene Oxide. *Chem. Eng. J.* **2012**, *204–206*, 258–263. [CrossRef]
15. Ren, X.; Chen, C.; Nagatsu, M.; Wang, X. Carbon Nanotubes as Adsorbents in Environmental Pollution Management: A Review. *Chem. Eng. J.* **2011**, *170*, 395–410. [CrossRef]
16. Gong, J.-L.; Wang, B.; Zeng, G.-M.; Yang, C.-P.; Niu, C.-G.; Niu, Q.-Y.; Zhou, W.-J.; Liang, Y. Removal of Cationic Dyes from Aqueous Solution Using Magnetic Multi-Wall Carbon Nanotube Nanocomposite as Adsorbent. *J. Hazard. Mater.* **2009**, *164*, 1517–1522. [CrossRef]
17. Deligeer, W.; Gao, Y.W.; Asuha, S. Adsorption of Methyl Orange on Mesoporous γ-Fe2O3/SiO2 Nanocomposites. *Appl. Surf. Sci.* **2011**, *257*, 3524–3528. [CrossRef]
18. Leodopoulos, C.; Doulia, D.; Gimouhopoulos, K.; Triantis, T.M. Single and Simultaneous Adsorption of Methyl Orange and Humic Acid onto Bentonite. *Appl. Clay Sci.* **2012**, *70*, 84–90. [CrossRef]
19. Amin, N.K. Removal of Direct Blue-106 Dye from Aqueous Solution Using New Activated Carbons Developed from Pomegranate Peel: Adsorption Equilibrium and Kinetics. *J. Hazard. Mater.* **2009**, *165*, 52–62. [CrossRef]
20. Ghaedi, M.; Taghavimoghadam, N.; Naderi, S.; Sahraei, R.; Daneshfar, A. Comparison of Removal of Bromothymol Blue from Aqueous Solution by Multiwalled Carbon Nanotube and $Zn(OH)_2$ Nanoparticles Loaded on Activated Carbon: A Thermodynamic Study. *J. Ind. Eng. Chem.* **2013**, *19*, 1493–1500. [CrossRef]
21. Li, Z.; Sun, Y.; Xing, J.; Meng, A. Fast Removal of Methylene Blue by Fe_3O_4 Magnetic Nanoparticles and Their Cycling Property. *J. Nanosci. Nanotechnol.* **2019**, *19*, 2116–2123. [CrossRef]
22. Ai, L.; Zhang, C.; Liao, F.; Wang, Y.; Li, M.; Meng, L.; Jiang, J. Removal of Methylene Blue from Aqueous Solution with Magnetite Loaded Multi-Wall Carbon Nanotube: Kinetic, Isotherm and Mechanism Analysis. *J. Hazard. Mater.* **2011**, *198*, 282–290. [CrossRef] [PubMed]
23. Habila, M.A.; Moshab, M.S.; El-Toni, A.M.; ALOthman, Z.A.; Badjah Hadj Ahmed, A.Y. Thermal Fabrication of Magnetic Fe_3O_4 (Nanoparticle)@Carbon Sheets from Waste Resources for the Adsorption of Dyes: Kinetic, Equilibrium, and UV–Visible Spectroscopy Investigations. *Nanomaterials* **2023**, *13*, 1266. [CrossRef] [PubMed]
24. Tishbi, P.; Mosayebi, M.; Salehi, Z.; Fatemi, S.; Faegh, E. Synthesizing Magnetic Graphene Oxide Nanomaterial (GO-Fe_3O4) and Kinetic Modelling of Methylene Blue Adsorption from Water. *Can. J. Chem. Eng.* **2022**, *100*, 3321–3334. [CrossRef]
25. Wu, K.-H.; Huang, W.-C.; Hung, W.-C.; Tsai, C.-W. Modified Expanded Graphite/Fe_3O_4 Composite as an Adsorbent of Methylene Blue: Adsorption Kinetics and Isotherms. *Mater. Sci. Eng. B* **2021**, *266*, 115068. [CrossRef]
26. Doan, L. Surface Modifications of Superparamagnetic Iron Oxide Nanoparticles with Polyvinyl Alcohol and Graphite as Methylene Blue Adsorbents. *Coatings* **2023**, *13*, 1558. [CrossRef]
27. Castro, C.S.; Guerreiro, M.C.; Gonçalves, M.; Oliveira, L.C.A.; Anastácio, A.S. Activated Carbon/Iron Oxide Composites for the Removal of Atrazine from Aqueous Medium. *J. Hazard. Mater.* **2009**, *164*, 609–614. [CrossRef]
28. Imamoglu, M.; Yıldız, H.; Altundag, H.; Turhan, Y. Efficient Removal of Cd(II) from Aqueous Solution by Dehydrated Hazelnut Husk Carbon. *J. Dispers. Sci. Technol.* **2015**, *36*, 284–290. [CrossRef]
29. Aygun, A.; Yenisoy-Karakas, S.; Duman, I. Production of Granular Activated Carbon from Fruit Stones and Nutshells and Evaluation of Their Physical, Chemical and Adsorption Properties. *Microporous Mesoporous Mater.* **2003**, *66*, 189–195. [CrossRef]
30. Senthilkumaar, S.; Varadarajan, P.R.; Porkodi, K.; Subbhuraam, C.V. Adsorption of Methylene Blue onto Jute Fiber Carbon: Kinetics and Equilibrium Studies. *J. Colloid. Interface Sci.* **2005**, *284*, 78–82. [CrossRef]
31. Kumar, P.S.; Ramalingam, S.; Sathishkumar, K. Removal of Methylene Blue Dye from Aqueous Solution by Activated Carbon Prepared from Cashew Nut Shell as a New Low-Cost Adsorbent. *Korean J. Chem. Eng.* **2011**, *28*, 149–155. [CrossRef]
32. Altundag, H.; Bina, E.; Altıntıg, E. The Levels of Trace Elements in Honey and Molasses Samples That Were Determined by ICP-OES After Microwave Digestion Method. *Biol. Trace Elem. Res.* **2016**, *170*, 508–514. [CrossRef] [PubMed]
33. Lelifajri; Nawi, M.A.; Sabar, S.; Supriatno; Nawawi, W.I. Preparation of Immobilized Activated Carbon-Polyvinyl Alcohol Composite for the Adsorptive Removal of 2,4-Dichlorophenoxyacetic Acid. *J. Water Process Eng.* **2018**, *25*, 269–277. [CrossRef]

34. Wang, J.; Li, M.; Zhou, S.; Xue, A.; Zhang, Y.; Zhao, Y.; Zhong, J.; Zhang, Q. Graphitic Carbon Nitride Nanosheets Embedded in Poly(Vinyl Alcohol) Nanocomposite Membranes for Ethanol Dehydration via Pervaporation. *Sep. Purif. Technol.* **2017**, *188*, 24–37. [CrossRef]
35. Hong, G.; Li, X.; Shen, L.; Wang, M.; Wang, C.; Yu, X.; Wang, X. High Recovery of Lead Ions from Aminated Polyacrylonitrile Nanofibrous Affinity Membranes with Micro/Nano Structure. *J. Hazard. Mater.* **2015**, *295*, 161–169. [CrossRef] [PubMed]
36. Alizadeh Fard, M.; Vosoogh, A.; Barkdoll, B.; Aminzadeh, B. Using Polymer Coated Nanoparticles for Adsorption of Micropollutants from Water. *Colloids Surf. Physicochem. Eng. Asp.* **2017**, *531*, 189–197. [CrossRef]
37. Wan Ismail, W.I.N.; Ain, S.K.; Zaharudin, R.; Jawad, A.H.; Ishak, M.A.M.; Ismail, K.; Sahid, S. New TiO_2/DSAT Immobilization System for Photodegradation of Anionic and Cationic Dyes. *Int. J. Photoenergy* **2015**, *2015*, 232741. [CrossRef]
38. Sabri, N.A.; Nawi, M.A.; Nawawi, W.I. Porous Immobilized C Coated N Doped TiO2 Containing In-Situ Generated Polyenes for Enhanced Visible Light Photocatalytic Activity. *Opt. Mater.* **2015**, *48*, 258–266. [CrossRef]
39. Tran, H.V.; Bui, L.T.; Dinh, T.T.; Le, D.H.; Huynh, C.D.; Trinh, A.X. Graphene Oxide/Fe_3O_4/Chitosan Nanocomposite: A Recoverable and Recyclable Adsorbent for Organic Dyes Removal. Application to Methylene Blue. *Mater. Res. Express* **2017**, *4*, 035701. [CrossRef]
40. Quach, T.P.T.; Doan, L. Surface Modifications of Superparamagnetic Iron Oxide Nanoparticles with Polyvinyl Alcohol, Chitosan, and Graphene Oxide as Methylene Blue Adsorbents. *Coatings* **2023**, *13*, 1333. [CrossRef]
41. Doan, L. Modifying Superparamagnetic Iron Oxide Nanoparticles as Methylene Blue Adsorbents: A Review. *ChemEngineering* **2023**, *7*, 77. [CrossRef]
42. Yusuf, M.S.; Sutriyo; Rahmasari, R. Synthesis Processing Condition Optimization of Citrate Stabilized Superparamagnetic Iron Oxide Nanoparticles Using Direct Co-Precipitation Method. *Biomed. Pharmacol. J.* **2021**, *14*, 1533–1542. [CrossRef]
43. Loh, K.-S.; Lee, Y.; Musa, A.; Salmah, A.; Zamri, I. Use of Fe_3O_4 Nanoparticles for Enhancement of Biosensor Response to the Herbicide 2,4-Dichlorophenoxyacetic Acid. *Sensors* **2008**, *8*, 5775–5791. [CrossRef]
44. Gong, J.; Lin, X. Facilitated Electron Transfer of Hemoglobin Embedded in Nanosized Fe_3O_4 Matrix Based on Paraffin Impregnated Graphite Electrode and Electrochemical Catalysis for Trichloroacetic Acid. *Microchem. J.* **2003**, *75*, 51–57. [CrossRef]
45. Liao, M.-H.; Chen, D.-H. Immobilization of Yeast Alcohol Dehydrogenase on Magnetic Nanoparticles for Improving Its Stability. *Biotechnol. Lett.* **2001**, *23*, 1723–1727. [CrossRef]
46. Deng, J.; Peng, Y.; He, C.; Long, X.; Li, P.; Chan, A.S.C. Magnetic and Conducting Fe_3O_4-Polypyrrole Nanoparticles with Core-Shell Structure. *Polym. Int.* **2003**, *52*, 1182–1187. [CrossRef]
47. Sodipo, B.K.; Aziz, A.A. A Sonochemical Approach to the Direct Surface Functionalization of Superparamagnetic Iron Oxide Nanoparticles with (3-Aminopropyl)Triethoxysilane. *Beilstein J. Nanotechnol.* **2014**, *5*, 1472–1476. [CrossRef] [PubMed]
48. Hwang, S.W.; Umar, A.; Dar, G.N.; Kim, S.H.; Badran, R.I. Synthesis and Characterization of Iron Oxide Nanoparticles for Phenyl Hydrazine Sensor Applications. *Sens. Lett.* **2014**, *12*, 97–101. [CrossRef]
49. Lopez, J.A.; González, F.; Bonilla, F.A.; Zambrano, G.; Gómez, M.E. Synthesis and Characterization of Fe_3O_4 Magnetic Nanofluid. *Rev. Latinoam. Metal. Mater.* **2010**, *30*, 60–66.
50. Adhikari, M.D.; Mukherjee, S.; Saikia, J.; Das, G.; Ramesh, A. Magnetic Nanoparticles for Selective Capture and Purification of an Antimicrobial Peptide Secreted by Food-Grade Lactic Acid Bacteria. *J. Mater. Chem. B* **2014**, *2*, 1432–1438. [CrossRef]
51. Ali, H.; Ismail, A.M. Fabrication of Magnetic Fe3O4/Polypyrrole/Carbon Black Nanocomposite for Effective Uptake of Congo Red and Methylene Blue Dye: Adsorption Investigation and Mechanism. *J. Polym. Environ.* **2023**, *31*, 976–998. [CrossRef]
52. Mahmoudi, M.; Simchi, A.; Milani, A.S.; Stroeve, P. Cell Toxicity of Superparamagnetic Iron Oxide Nanoparticles. *J. Colloid. Interface Sci.* **2009**, *336*, 510–518. [CrossRef] [PubMed]
53. Mahmoudi, M.; Simchi, A.; Imani, M.; Milani, A.S.; Stroeve, P. Optimal Design and Characterization of Superparamagnetic Iron Oxide Nanoparticles Coated with Polyvinyl Alcohol for Targeted Delivery and Imaging. *J. Phys. Chem. B* **2008**, *112*, 14470–14481. [CrossRef] [PubMed]
54. Kostyukova, D.; Chung, Y.H. Synthesis of Iron Oxide Nanoparticles Using Isobutanol. *J. Nanomater.* **2016**, *2016*, 4982675. [CrossRef]
55. Kharazmi, A.; Faraji, N.; Mat Hussin, R.; Saion, E.; Yunus, W.M.M.; Behzad, K. Structural, Optical, Opto-Thermal and Thermal Properties of ZnS–PVA Nanofluids Synthesized through a Radiolytic Approach. *Beilstein J. Nanotechnol.* **2015**, *6*, 529–536. [CrossRef]
56. Bhat, N.V.; Nate, M.M.; Kurup, M.B.; Bambole, V.A.; Sabharwal, S. Effect of γ-Radiation on the Structure and Morphology of Polyvinyl Alcohol Films. *Nucl. Instrum. Methods Phys. Res. Sect. B Beam Interact. Mater. At.* **2005**, *237*, 585–592. [CrossRef]
57. Lee, J.; Isobe, T.; Senna, M. Preparation of Ultrafine Fe_3O_4 Particles by Precipitation in the Presence of PVA at High pH. *J. Colloid. Interface Sci.* **1996**, *177*, 490–494. [CrossRef]
58. Korbag, I.; Mohamed Saleh, S. Studies on the Formation of Intermolecular Interactions and Structural Characterization of Polyvinyl Alcohol/Lignin Film. *Int. J. Environ. Stud.* **2016**, *73*, 226–235. [CrossRef]
59. Tang, C.; Shu, Y.; Zhang, R.; Li, X.; Song, J.; Li, B.; Zhang, Y.; Ou, D. Comparison of the Removal and Adsorption Mechanisms of Cadmium and Lead from Aqueous Solution by Activated Carbons Prepared from Typha Angustifolia and Salix Matsudana. *RSC Adv.* **2017**, *7*, 16092–16103. [CrossRef]

60. Pochapski, D.J.; Carvalho dos Santos, C.; Leite, G.W.; Pulcinelli, S.H.; Santilli, C.V. Zeta Potential and Colloidal Stability Predictions for Inorganic Nanoparticle Dispersions: Effects of Experimental Conditions and Electrokinetic Models on the Interpretation of Results. *Langmuir* **2021**, *37*, 13379–13389. [CrossRef]
61. Bondarenko, L.S.; Kovel, E.S.; Kydralieva, K.A.; Dzhardimalieva, G.I.; Illés, E.; Tombácz, E.; Kicheeva, A.G.; Kudryasheva, N.S. Effects of Modified Magnetite Nanoparticles on Bacterial Cells and Enzyme Reactions. *Nanomaterials* **2020**, *10*, 1499. [CrossRef]
62. Soares, S.F.; Fernandes, T.; Trindade, T.; Daniel-da-Silva, A.L. Trimethyl Chitosan/Siloxane-Hybrid Coated Fe_3O_4 Nanoparticles for the Uptake of Sulfamethoxazole from Water. *Molecules* **2019**, *24*, 1958. [CrossRef] [PubMed]
63. Wee, S.-B.; Oh, H.-C.; Kim, T.-G.; An, G.-S.; Choi, S.-C. Role of N-Methyl-2-Pyrrolidone for Preparation of Fe_3O_4@SiO_2 Controlled the Shell Thickness. *J. Nanoparticle Res.* **2017**, *19*, 143. [CrossRef]
64. Ma, P.; Luo, Q.; Chen, J.; Gan, Y.; Du, J.; Ding, S.; Xi, Z.; Yang, X. Intraperitoneal Injection of Magnetic Fe_3O_4-Nanoparticle Induces Hepatic and Renal Tissue Injury via Oxidative Stress in Mice. *Int. J. Nanomed.* **2012**, *7*, 4809–4818. [CrossRef]
65. Ferrah, N. Comparative Study of Mercury(II) Species Removal onto Naked and Modified Magnetic Chitosan Flakes Coated Ethylenediaminetetraacetic-Disodium: Kinetic and Thermodynamic Modeling. *Environ. Sci. Pollut. Res.* **2018**, *25*, 24923–24938. [CrossRef] [PubMed]
66. Meng, X.; Ryu, J.; Kim, B.; Ko, S. Application of Iron Oxide as a pH-Dependent Indicator for Improving the Nutritional Quality. *Clin. Nutr. Res.* **2016**, *5*, 172. [CrossRef]
67. Zhu, A.; Yuan, L.; Liao, T. Suspension of Fe3O4 Nanoparticles Stabilized by Chitosan and O-Carboxymethylchitosan. *Int. J. Pharm.* **2008**, *350*, 361–368. [CrossRef]
68. Sotomayor, F.J.; Cychosz, K.A.; Thommes, M. Characterization of Micro/Mesoporous Materials by Physisorption: Concepts and Case Studies. *Acc. Mater. Surf. Res.* **2018**, *3*, 34–50.
69. Thommes, M.; Kaneko, K.; Neimark, A.V.; Olivier, J.P.; Rodriguez-Reinoso, F.; Rouquerol, J.; Sing, K.S.W. Physisorption of Gases, with Special Reference to the Evaluation of Surface Area and Pore Size Distribution (IUPAC Technical Report). *Pure Appl. Chem.* **2015**, *87*, 1051–1069. [CrossRef]
70. Paramarta, V.; Kristianto, Y.; Taufik, A.; Saleh, R. Improve Sonocatalytic Performance Using Modified Semiconductor Catalyst SnO_2 and ZrO_2 by Magnetite Materials. *IOP Conf. Ser. Mater. Sci. Eng.* **2017**, *188*, 012042. [CrossRef]
71. Esmaeili, H.; Tamjidi, S. Ultrasonic-Assisted Synthesis of Natural Clay/Fe_3O_4/Graphene Oxide for Enhance Removal of Cr (VI) from Aqueous Media. *Environ. Sci. Pollut. Res.* **2020**, *27*, 31652–31664. [CrossRef]
72. DemiRel Topel, S.; Gürkan Polat, T. pH-RESPONSIVE CARBOXYMETHYL CELLULOSE CONJUGATED SUPERPARAMAGNETIC IRON OXIDE NANOCARRIERS. *J. Sci. Perspect.* **2019**, *3*, 99–110. [CrossRef]
73. Munasir; Kusumawati, R.P. Synthesis and Characterization of Fe_3O_4@rGO Composite with Wet-Mixing (Ex-Situ) Process. *J. Phys. Conf. Ser.* **2019**, *1171*, 012048. [CrossRef]
74. Norouzian Baghani, A.; Mahvi, A.H.; Gholami, M.; Rastkari, N.; Delikhoon, M. One-Pot Synthesis, Characterization and Adsorption Studies of Amine-Functionalized Magnetite Nanoparticles for Removal of Cr (VI) and Ni (II) Ions from Aqueous Solution: Kinetic, Isotherm and Thermodynamic Studies. *J. Environ. Health Sci. Eng.* **2016**, *14*, 11. [CrossRef] [PubMed]
75. Heydari Sheikh Hossein, H.; Jabbari, I.; Zarepour, A.; Zarrabi, A.; Ashrafizadeh, M.; Taherian, A.; Makvandi, P. Functionalization of Magnetic Nanoparticles by Folate as Potential MRI Contrast Agent for Breast Cancer Diagnostics. *Molecules* **2020**, *25*, 4053. [CrossRef] [PubMed]
76. Yao, Y.; Miao, S.; Liu, S.; Ma, L.P.; Sun, H.; Wang, S. Synthesis, Characterization, and Adsorption Properties of Magnetic Fe_3O_4@graphene Nanocomposite. *Chem. Eng. J.* **2012**, *184*, 326–332. [CrossRef]
77. Yao, Y.; Xu, F.; Chen, M.; Xu, Z.; Zhu, Z. Adsorption Behavior of Methylene Blue on Carbon Nanotubes. *Bioresour. Technol.* **2010**, *101*, 3040–3046. [CrossRef]
78. Pigatto, G.; Lodi, A.; Finocchio, E.; Palma, M.S.A.; Converti, A. Chitin as Biosorbent for Phenol Removal from Aqueous Solution: Equilibrium, Kinetic and Thermodynamic Studies. *Chem. Eng. Process. Process Intensif.* **2013**, *70*, 131–139. [CrossRef]
79. Seki, Y.; Yurdakoç, K. Adsorption of Promethazine Hydrochloride with KSF Montmorillonite. *Adsorption* **2006**, *12*, 89–100. [CrossRef]
80. Sharma, P.; Kaur, R.; Baskar, C.; Chung, W.-J. Removal of Methylene Blue from Aqueous Waste Using Rice Husk and Rice Husk Ash. *Desalination* **2010**, *259*, 249–257. [CrossRef]
81. Peydayesh, M.; Rahbar-Kelishami, A. Adsorption of Methylene Blue onto Platanus Orientalis Leaf Powder: Kinetic, Equilibrium and Thermodynamic Studies. *J. Ind. Eng. Chem.* **2015**, *21*, 1014–1019. [CrossRef]
82. Nekouei, F.; Nekouei, S.; Tyagi, I.; Gupta, V.K. Kinetic, Thermodynamic and Isotherm Studies for Acid Blue 129 Removal from Liquids Using Copper Oxide Nanoparticle-Modified Activated Carbon as a Novel Adsorbent. *J. Mol. Liq.* **2015**, *201*, 124–133. [CrossRef]
83. Luo, X.-P.; Fu, S.-Y.; Du, Y.-M.; Guo, J.-Z.; Li, B. Adsorption of Methylene Blue and Malachite Green from Aqueous Solution by Sulfonic Acid Group Modified MIL-101. *Microporous Mesoporous Mater.* **2017**, *237*, 268–274. [CrossRef]
84. Sharma, P.; Hussain, N.; Borah, D.J.; Das, M.R. Kinetics and Adsorption Behavior of the Methyl Blue at the Graphene Oxide/Reduced Graphene Oxide Nanosheet–Water Interface: A Comparative Study. *J. Chem. Eng. Data* **2013**, *58*, 3477–3488. [CrossRef]
85. Ai, L.; Li, M.; Li, L. Adsorption of Methylene Blue from Aqueous Solution with Activated Carbon/Cobalt Ferrite/Alginate Composite Beads: Kinetics, Isotherms, and Thermodynamics. *J. Chem. Eng. Data* **2011**, *56*, 3475–3483. [CrossRef]

86. Karaer, H.; Kaya, İ. Synthesis, Characterization of Magnetic Chitosan/Active Charcoal Composite and Using at the Adsorption of Methylene Blue and Reactive Blue4. *Microporous Mesoporous Mater.* **2016**, *232*, 26–38. [CrossRef]
87. Singh, D. Studies of the Adsorption Thermodynamics of Oxamyl on Fly Ash. *Adsorpt. Sci. Technol.* **2000**, *18*, 741–748. [CrossRef]
88. Özcan, A.; Öncü, E.M.; Özcan, A.S. Kinetics, Isotherm and Thermodynamic Studies of Adsorption of Acid Blue 193 from Aqueous Solutions onto Natural Sepiolite. *Colloids Surf. Physicochem. Eng. Asp.* **2006**, *277*, 90–97. [CrossRef]
89. Bhattacharyya, K.G.; Sharma, A. Kinetics and Thermodynamics of Methylene Blue Adsorption on Neem (Azadirachta Indica) Leaf Powder. *Dye. Pigment.* **2005**, *65*, 51–59. [CrossRef]
90. Umoren, S.A.; Etim, U.J.; Israel, A.U. Adsorption of Methylene Blue from Industrial Effluent Using Poly (Vinyl Alcohol). *J. Mater. Environ. Sci.* **2013**, *4*, 75–86.
91. Ofomaja, A.E.; Ho, Y.-S. Equilibrium Sorption of Anionic Dye from Aqueous Solution by Palm Kernel Fibre as Sorbent. *Dye. Pigment.* **2007**, *74*, 60–66. [CrossRef]
92. Dai, H.; Huang, Y.; Huang, H. Eco-Friendly Polyvinyl Alcohol/Carboxymethyl Cellulose Hydrogels Reinforced with Graphene Oxide and Bentonite for Enhanced Adsorption of Methylene Blue. *Carbohydr. Polym.* **2018**, *185*, 1–11. [CrossRef] [PubMed]
93. Bulut, Y.; Aydın, H. A Kinetics and Thermodynamics Study of Methylene Blue Adsorption on Wheat Shells. *Desalination* **2006**, *194*, 259–267. [CrossRef]
94. Dai, H.; Huang, H. Synthesis, Characterization and Properties of Pineapple Peel Cellulose-g-Acrylic Acid Hydrogel Loaded with Kaolin and Sepia Ink. *Cellulose* **2017**, *24*, 69–84. [CrossRef]
95. Sekhavat Pour, Z.; Ghaemy, M. Removal of Dyes and Heavy Metal Ions from Water by Magnetic Hydrogel Beads Based on Poly(Vinyl Alcohol)/Carboxymethyl Starch-g-Poly(Vinyl Imidazole). *RSC Adv.* **2015**, *5*, 64106–64118. [CrossRef]
96. Sharma, G.; Naushad, M.; Al-Muhtaseb, A.H.; Kumar, A.; Khan, M.R.; Kalia, S.; Shweta; Bala, M.; Sharma, A. Fabrication and Characterization of Chitosan-Crosslinked-Poly(Alginic Acid) Nanohydrogel for Adsorptive Removal of Cr(VI) Metal Ion from Aqueous Medium. *Int. J. Biol. Macromol.* **2017**, *95*, 484–493. [CrossRef]
97. Sharma, G.; Kumar, A.; Devi, K.; Sharma, S.; Naushad, M.; Ghfar, A.A.; Ahamad, T.; Stadler, F.J. Guar Gum-Crosslinked-Soya Lecithin Nanohydrogel Sheets as Effective Adsorbent for the Removal of Thiophanate Methyl Fungicide. *Int. J. Biol. Macromol.* **2018**, *114*, 295–305. [CrossRef]
98. Sharma, G.; Kumar, A.; Naushad, M.; García-Peñas, A.; Al-Muhtaseb, A.H.; Ghfar, A.A.; Sharma, V.; Ahamad, T.; Stadler, F.J. Fabrication and Characterization of Gum Arabic-Cl-Poly(Acrylamide) Nanohydrogel for Effective Adsorption of Crystal Violet Dye. *Carbohydr. Polym.* **2018**, *202*, 444–453. [CrossRef]
99. Ma, J.; Huang, D.; Zou, J.; Li, L.; Kong, Y.; Komarneni, S. Adsorption of Methylene Blue and Orange II Pollutants on Activated Carbon Prepared from Banana Peel. *J. Porous Mater.* **2015**, *22*, 301–311. [CrossRef]
100. Hameed, B.H.; Din, A.T.M.; Ahmad, A.L. Adsorption of Methylene Blue onto Bamboo-Based Activated Carbon: Kinetics and Equilibrium Studies. *J. Hazard. Mater.* **2007**, *141*, 819–825. [CrossRef]
101. Theydan, S.K.; Ahmed, M.J. Adsorption of Methylene Blue onto Biomass-Based Activated Carbon by FeCl3 Activation: Equilibrium, Kinetics, and Thermodynamic Studies. *J. Anal. Appl. Pyrolysis* **2012**, *97*, 116–122. [CrossRef]
102. Hameed, B.H.; Ahmad, A.L.; Latiff, K.N.A. Adsorption of Basic Dye (Methylene Blue) onto Activated Carbon Prepared from Rattan Sawdust. *Dye. Pigment.* **2007**, *75*, 143–149. [CrossRef]
103. Bestani, B.; Benderdouche, N.; Benstaali, B.; Belhakem, M.; Addou, A. Methylene Blue and Iodine Adsorption onto an Activated Desert Plant. *Bioresour. Technol.* **2008**, *99*, 8441–8444. [CrossRef] [PubMed]
104. El Qada, E.N.; Allen, S.J.; Walker, G.M. Adsorption of Methylene Blue onto Activated Carbon Produced from Steam Activated Bituminous Coal: A Study of Equilibrium Adsorption Isotherm. *Chem. Eng. J.* **2006**, *124*, 103–110. [CrossRef]
105. Foo, K.Y.; Hameed, B.H. Microwave-Assisted Preparation of Oil Palm Fiber Activated Carbon for Methylene Blue Adsorption. *Chem. Eng. J.* **2011**, *166*, 792–795. [CrossRef]
106. Belhachemi, M.; Addoun, F. Comparative Adsorption Isotherms and Modeling of Methylene Blue onto Activated Carbons. *Appl. Water Sci.* **2011**, *1*, 111–117. [CrossRef]
107. Deng, H.; Yang, L.; Tao, G.; Dai, J. Preparation and Characterization of Activated Carbon from Cotton Stalk by Microwave Assisted Chemical Activation—Application in Methylene Blue Adsorption from Aqueous Solution. *J. Hazard. Mater.* **2009**, *166*, 1514–1521. [CrossRef]
108. Vargas, A.M.M.; Cazetta, A.L.; Kunita, M.H.; Silva, T.L.; Almeida, V.C. Adsorption of Methylene Blue on Activated Carbon Produced from Flamboyant Pods (Delonix Regia): Study of Adsorption Isotherms and Kinetic Models. *Chem. Eng. J.* **2011**, *168*, 722–730. [CrossRef]
109. Wang, S.; Boyjoo, Y.; Choueib, A. A Comparative Study of Dye Removal Using Fly Ash Treated by Different Methods. *Chemosphere* **2005**, *60*, 1401–1407. [CrossRef]
110. Tsai, W.T.; Yang, J.M.; Lai, C.W.; Cheng, Y.H.; Lin, C.C.; Yeh, C.W. Characterization and Adsorption Properties of Eggshells and Eggshell Membrane. *Bioresour. Technol.* **2006**, *97*, 488–493. [CrossRef]
111. Banerjee, S.; Dastidar, M.G. Use of Jute Processing Wastes for Treatment of Wastewater Contaminated with Dye and Other Organics. *Bioresour. Technol.* **2005**, *96*, 1919–1928. [CrossRef]
112. Garg, V.K.; Amita, M.; Kumar, R.; Gupta, R. Basic Dye (Methylene Blue) Removal from Simulated Wastewater by Adsorption Using Indian Rosewood Sawdust: A Timber Industry Waste. *Dye. Pigment.* **2004**, *63*, 243–250. [CrossRef]

113. Fytianos, K.; Voudrias, E.; Kokkalis, E. Sorption–Desorption Behaviour of 2,4-Dichlorophenol by Marine Sediments. *Chemosphere* **2000**, *40*, 3–6. [CrossRef]
114. Reed, B.E.; Matsumoto, M.R. Modeling Cadmium Adsorption by Activated Carbon Using the Langmuir and Freundlich Isotherm Expressions. *Sep. Sci. Technol.* **1993**, *28*, 2179–2195. [CrossRef]
115. Samrot, A.V.; Ali, H.H.; Selvarani, J.; Faradjeva, E.; Raji, P.; Prakash, P.; Kumar S, S. Adsorption Efficiency of Chemically Synthesized Superparamagnetic Iron Oxide Nanoparticles (SPIONs) on Crystal Violet Dye. *Curr. Res. Green. Sustain. Chem.* **2021**, *4*, 100066. [CrossRef]
116. Üner, O.; Geçgel, Ü.; Bayrak, Y. Adsorption of Methylene Blue by an Efficient Activated Carbon Prepared from Citrullus Lanatus Rind: Kinetic, Isotherm, Thermodynamic, and Mechanism Analysis. *Water. Air. Soil. Pollut.* **2016**, *227*, 247. [CrossRef]
117. Sheha, R.R.; Metwally, E. Equilibrium Isotherm Modeling of Cesium Adsorption onto Magnetic Materials. *J. Hazard. Mater.* **2007**, *143*, 354–361. [CrossRef] [PubMed]
118. Chabani, M.; Amrane, A.; Bensmaili, A. Kinetic Modelling of the Adsorption of Nitrates by Ion Exchange Resin. *Chem. Eng. J.* **2006**, *125*, 111–117. [CrossRef]
119. Özcan, A.; Özcan, A.S.; Tunali, S.; Akar, T.; Kiran, I. Determination of the Equilibrium, Kinetic and Thermodynamic Parameters of Adsorption of Copper(II) Ions onto Seeds of Capsicum Annuum. *J. Hazard. Mater.* **2005**, *124*, 200–208. [CrossRef]
120. Helfferich, F.G. *Ion Exchange*; Courier Corporation: Chelmsford, MA, USA, 1995; ISBN 978-0-486-68784-1.
121. Onyango, M.S.; Kojima, Y.; Aoyi, O.; Bernardo, E.C.; Matsuda, H. Adsorption Equilibrium Modeling and Solution Chemistry Dependence of Fluoride Removal from Water by Trivalent-Cation-Exchanged Zeolite F-9. *J. Colloid. Interface Sci.* **2004**, *279*, 341–350. [CrossRef]
122. Tan, I.A.W.; Ahmad, A.L.; Hameed, B.H. Adsorption of Basic Dye on High-Surface-Area Activated Carbon Prepared from Coconut Husk: Equilibrium, Kinetic and Thermodynamic Studies. *J. Hazard. Mater.* **2008**, *154*, 337–346. [CrossRef]
123. Liu, Y.; Bai, Q.; Lou, S.; Di, D.; Li, J.; Guo, M. Adsorption Characteristics of (−)-Epigallocatechin Gallate and Caffeine in the Extract of Waste Tea on Macroporous Adsorption Resins Functionalized with Chloromethyl, Amino, and Phenylamino Groups. *J. Agric. Food Chem.* **2012**, *60*, 1555–1566. [CrossRef] [PubMed]
124. Al-Ghouti, M.A.; Da'ana, D.A. Guidelines for the Use and Interpretation of Adsorption Isotherm Models: A Review. *J. Hazard. Mater.* **2020**, *393*, 122383. [CrossRef] [PubMed]
125. Jawad, A.H.; Surip, S.N. Upgrading Low Rank Coal into Mesoporous Activated Carbon via Microwave Process for Methylene Blue Dye Adsorption: Box Behnken Design and Mechanism Study. *Diam. Relat. Mater.* **2022**, *127*, 109199. [CrossRef]
126. Jawad, A.H.; Ismail, K.; Ishak, M.A.M.; Wilson, L.D. Conversion of Malaysian Low-Rank Coal to Mesoporous Activated Carbon: Structure Characterization and Adsorption Properties. *Chin. J. Chem. Eng.* **2019**, *27*, 1716–1727. [CrossRef]
127. Jawad, A.H.; Mohd Firdaus Hum, N.N.; Abdulhameed, A.S.; Mohd Ishak, M.A. Mesoporous Activated Carbon from Grass Waste via H_3PO_4-Activation for Methylene Blue Dye Removal: Modelling, Optimisation, and Mechanism Study. *Int. J. Environ. Anal. Chem.* **2020**, *102*, 6061–6077. [CrossRef]
128. Kannan, N.; Sundaram, M.M. Kinetics and Mechanism of Removal of Methylene Blue by Adsorption on Various Carbons—A Comparative Study. *Dye. Pigment.* **2001**, *51*, 25–40. [CrossRef]

Disclaimer/Publisher's Note: The statements, opinions and data contained in all publications are solely those of the individual author(s) and contributor(s) and not of MDPI and/or the editor(s). MDPI and/or the editor(s) disclaim responsibility for any injury to people or property resulting from any ideas, methods, instructions or products referred to in the content.